



Removal of Cr(VI) by 3D TiO₂-graphene hydrogel via adsorption enriched with photocatalytic reduction

Yao Li^{a,*}, Wenquan Cui^{a,*}, Li Liu^a, Ruilong Zong^b, Wenqing Yao^b, Yinghua Liang^a, Yongfa Zhu^{b,**}

^a College of Chemical Engineering, Hebei Key Laboratory for Environment Photocatalytic and Electrocatalytic Materials, North China University of Science and Technology, Tangshan, Hebei 063009, PR China

^b Department of Chemistry, Tsinghua University, Beijing 100084, China

ARTICLE INFO

Article history:

Received 15 March 2016

Received in revised form 12 May 2016

Accepted 22 June 2016

Available online 22 June 2016

Keywords:

TiO₂-rGH composite hydrogel

3D structure

Adsorption-photocatalysis

Cr (VI) removal

ABSTRACT

A novel method for removing Cr(VI) from aqueous solutions used a TiO₂-graphene hydrogel with three-dimensional (3D) network structure. Graphene is capable of non-porous surface adsorption and π - π interaction adsorption. The combination between graphene and TiO₂ nanospheres promoted photo-induced charge transport and separation, thereby facilitating photocatalytic reduction of Cr(VI). For TiO₂-rGH, the synergy of adsorption and photocatalysis played an important role in removing Cr(VI) from aqueous solutions. The TiO₂-rGH material exhibited superb adsorption-photocatalysis performance, removing 100% Cr(VI) from a solution containing (5 mg/L) within 30 min under UV irradiation. Under continuous flow conditions, the adsorption-photocatalytic activity of TiO₂-rGH was well maintained and the Cr(VI)-removing percentage was kept at 100% for a prolonged period until the breakthrough point was reached.

© 2016 Elsevier B.V. All rights reserved.

1. Introduction

Cr(VI) is a common heavy metal contaminate because of its high toxicity and bio-accumulativity. It is carcinogenic and thus is a threat to human healthy [1]. A rich array of physical and chemical approaches including ion exchange [2], chemical precipitation [3], electro-reduction [4], and membrane separation [5] have been developed for removing chromium from industrial waste. However, most of these methods suffer from drawbacks such as low efficiency, high cost, generation of secondary pollution, and incapability of removing trace contaminants, thereby limiting practical applications. Notably, adsorption [6] and photocatalysis [7] have been shown to be superior to other techniques in chromium removal and thus are widely used and extensively researched.

Treating industrial heavy metal waste using the adsorption method with high speed, adaptability, and efficiency has exhibited great potential and attracted the attention of industrial and scientific communities. Effective adsorption can be achieved via a large contact area and a strong interaction between the adsorbent mate-

rial and the heavy metal ions. However, conventional adsorbent material such as activated carbon [8], zeolite [9], carbon fibers [10], natural diatomaceous earth [11], etc., mainly rely on adsorption active sites and interlayer adsorption sites within the pores. This limits the adsorption capacity and adsorption rate, and renders the adsorbent material easily saturated.

Compared to other chemical methods, the photocatalytic method [12] displays many advantages in removing toxic heavy metal ions, including high efficiency, low energy consumption, and mild reaction conditions, which are the key points for removing Cr(VI) pollution from water. However, the photocatalyst usually has limitations of surface area and low adsorption capacity. Moreover, the powder form of photocatalyst limits recycling of catalyst and repeated reuse. Therefore, it is highly demanded to develop new methods to overcome the limitations for both adsorption and photocatalysis, so that improve their performance in removing Cr(VI) from water.

In this work, we aimed to develop a combinational approach based on both the adsorption method and the photocatalytic method and test its performance in removing Cr(VI) from aqueous solution. Graphene, a hierarchical structure of carbon-based material [13], has attracted a lot of interest in recent years because of its unique non-porous surface adsorption and π - π interaction adsorption characteristics [14]. However, when graphene nanosheets are

* Corresponding author.

** Corresponding author.

E-mail addresses: wkcui@163.com (W. Cui), zhuyf@mail.tsinghua.edu.cn (Y. Zhu).

assembled into 2D macrostructures, the accessible surface area of those nano-sheets is not optimized [15] as graphene nanosheets are prone to aggregate and restack. In order to solve this problem, three-dimensional (3D) graphene macrostructures, such as hydrogels and aerogels, have been developed. The 3D graphene-based macro-structures [16] not only increase the accessible surface area of the graphene nano-sheets but also have highly porous structures with pore sizes of several micrometers, capable of rapid adsorption. Previous reports [17,18] revealed that the graphene hydrogel showed high adsorption rate, large adsorption capacity, and free separation in the adsorption of removing pollutant from water.

Herein, we prepared a composite material of TiO_2 and reduced graphene oxide hydrogel (rGH), TiO_2 -rGH, and performed its removing ability of toxic Cr(VI) from the water solution. The TiO_2 -rGH exhibited a large surface area and interconnected pores in the 3D hydrogel structure which provide abundant active sites for adsorption and crossed diffusion channels for adsorbate molecules. The adsorbed Cr(VI) in TiO_2 -rGH 3D structure could then be fast reduced to Cr(III) by photocatalysis over TiO_2 nano-particles which modified in the rGH 3D structure. The synergistic effect of played an important role in rapidly and efficiently removing Cr(VI) . The TiO_2 -rGH 3D structure showed the superiority for separation free in the continuous flow system for removing of Cr(VI) via the combined adsorption & photocatalysis.

2. Experimental methods

2.1. Synthesis of TiO_2 -rGH

2.1.1. Synthesis of rGH

Graphite oxide (GO) was synthesized by a method modified from the Hummers method [19]. Graphite (6.0 g) was mixed with 140 mL of H_2SO_4 (98 wt%) in a flask and stirred for 10 min on an ice bath. NaNO_3 (3.0 g) and KMnO_4 (18.0 g) were added into the flask. The reaction mixture was stirred at 20°C for 3 h. Then the reaction temperature was increased to 35°C . After 4 h, the reaction mixture was diluted slowly with 300 mL of water and the reaction temperature was rapidly increased to 95°C . After another 2 h, 600 mL of water and 40 mL of H_2O_2 (30 wt%) were titrated into the reaction system. The sample was centrifuged and the pellet was collected. The pellet was washed with 10% HCl, and then dialyzed against water for 7 days. After another round of centrifugation, the resulting pellet was GO.

rGH was synthesized using a method slightly modified from a procedure reported in the literature [20]. GO and sodium ascorbate were mixed at a 1:10 ratio. The mixture was stirred for 10 min. Then the reaction temperature was increased to 95°C . After 1 h, rGH was obtained. The obtained rGH was washed for several times by deionized water and dehydrated by the freeze-drying process during 24 h.

2.1.2. Synthesis of TiO_2 -rGH

TiO_2 (P25) nanopowders were supplied by Degussa, which is known as one of the best TiO_2 photocatalysts and used frequently as a benchmark in photocatalysis.

The synthesis of TiO_2 -rGH was as follows: TiO_2 was mixed with an equal volume of polyethylene glycol (PEG) 200 and the mixture was grinded to allow for fully mixing. GO was added into the mixture, followed by ultra-sonication for about 30 min. Then sodium ascorbate was added into the mixture. The resulting mixture was stirred for 30 min and heated at 95°C for 60 min to obtain TiO_2 -rGH. Finally, the obtained TiO_2 -rGH hydrogel was washed thoroughly with deionized water for several times to remove the PEG, and then dehydrated by the freeze-drying process during 24 h.

For comparison, TiO_2 combined with activated carbon (AC, Sigma-Aldrich) and Al_2O_3 (Alfa Aesar) composites were also prepared via impregnation-calcination process.

2.2. Characterization of TiO_2 -rGH

The crystal structure and phase state of TiO_2 -rGH were determined by X-ray diffractometry (XRD) using a Rigaku D/MAX2500 PC diffractometer with $\text{Cu K}\alpha$ radiation, at an operating voltage of 40 kV, an operating current of 100 mA, and a scanning range from 5 to 80° . The morphology and size of the sample were imaged with scanning electron microscopy (SEM) using a Hitachi s-4800 SEM microscope and with transmission electron microscopy (TEM) using a JEOL JEM-2010 TEM microscope. Raman spectra were recorded on a microscopic confocal Raman spectrometer (Thermo Electron DXR) with an excitation wavelength at 524 nm. The Fourier transform infrared (FTIR) spectra of the samples were recorded on a Thermo Nicolet Avatar 370 spectrometer. The Brunauer-Emmett-Teller (BET) specific surface area of the sample was characterized by nitrogen adsorption at 77 K with a Micromeritics 3020 instrument. The chemical states of the photocatalysts were analyzed by X-ray photoelectron spectroscopy (XPS) using an XSAM800 apparatus. The Zeta potential measurements were made with a Delsa Nano C zeta potential instrument (Beckman Coulter).

2.3. Synergy of adsorption and photocatalysis in removing Cr(VI)

2.3.1. Static system:

Adsorption performance of TiO_2 -rGH: $\text{K}_2\text{Cr}_2\text{O}_7$ was dissolved in deionized water, and the pH of the solution is about 5.5. TiO_2 -rGH (100 mg) was placed in a 250 mL Erlenmeyer flask. The Cr(VI) solution (100 mL) was added into the flask. The temperature was maintained at $25 \pm 2^\circ\text{C}$ and the flask was shaken at a speed of 200 r/min. A 3 mL aliquot of the suspension mixture was taken at intervals, and filtered with a filter membrane ($0.45 \mu\text{m}$). The concentration of the Cr ion in the solution phase was determined.

2.3.2. Elution and desorption

The TiO_2 -rGH sample that reached adsorption saturation was washed by 0.5 M HNO_3 at the flow rate of 6.4 mL/min. A 3 mL aliquot of the suspension mixture was taken at intervals, and filtered with a filter membrane ($0.45 \mu\text{m}$). The concentration of the Cr ion in the solution phase was determined.

2.3.3. Photocatalytic reduction of Cr(VI)

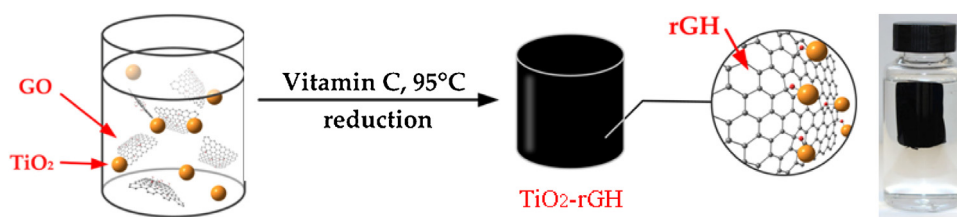
Photocatalytic reduction of Cr(VI) were performed using a vertical radiation method. A 250 W mercury lamp (model: XC-ZD400G, main wavelength: 365 nm) was placed at a distance of 10 cm above the glass reactor. The temperature of the glass reactor was maintained at $25 \pm 2^\circ\text{C}$ by circulating water. TiO_2 -rGH (100 mg) and the Cr(VI) solution (100 mL) were added into the reactor. After incubation in the dark, the catalyst reached the adsorption equilibrium. Then the photocatalysis process was initiated by turning on the mercury lamp. A 3 mL aliquot of the reaction mixture was taken at intervals, and filtered with a filter membrane ($0.45 \mu\text{m}$). The concentration of the Cr ion in the solution phase was determined.

2.3.4. Cycle performance of TiO_2 -rGH

After each usage cycle, the TiO_2 -rGH material was isolated by filtration. Then it was employed to treat a fresh Cr(VI) solution containing the same initial concentration of Cr(IV) (10 mg/L).

2.3.5. Continues flow reaction – synergy of photocatalysis and adsorption in removing Cr(VI)

The performance of the TiO_2 -rGH composite material in removing Cr(VI) under continuous flow conditions was further studied



Scheme 1. Schematic illustration of the preparation process of TiO₂-rGH.

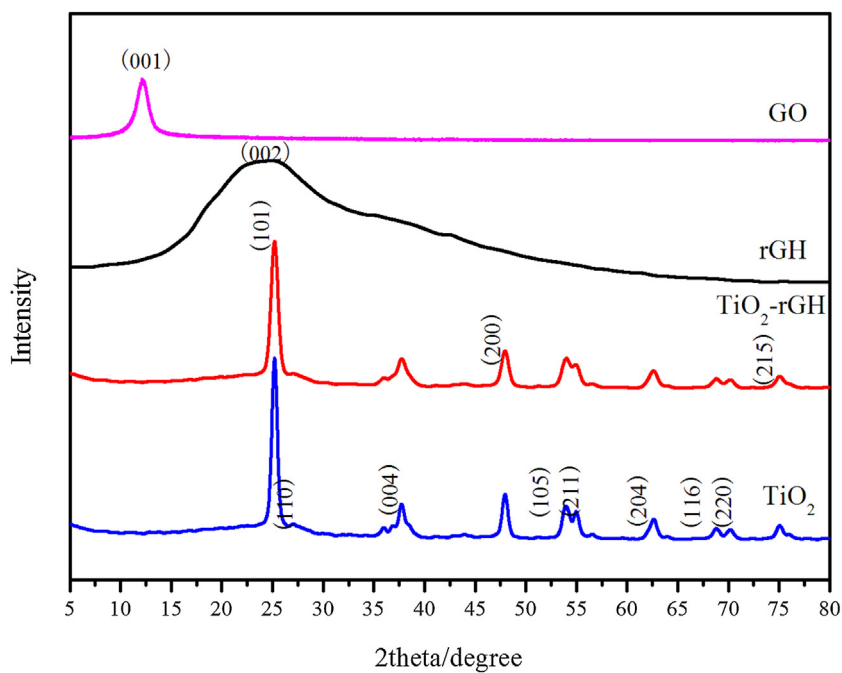


Fig. 1. XRD spectra of GO, rGH, TiO₂, and TiO₂-rGH.

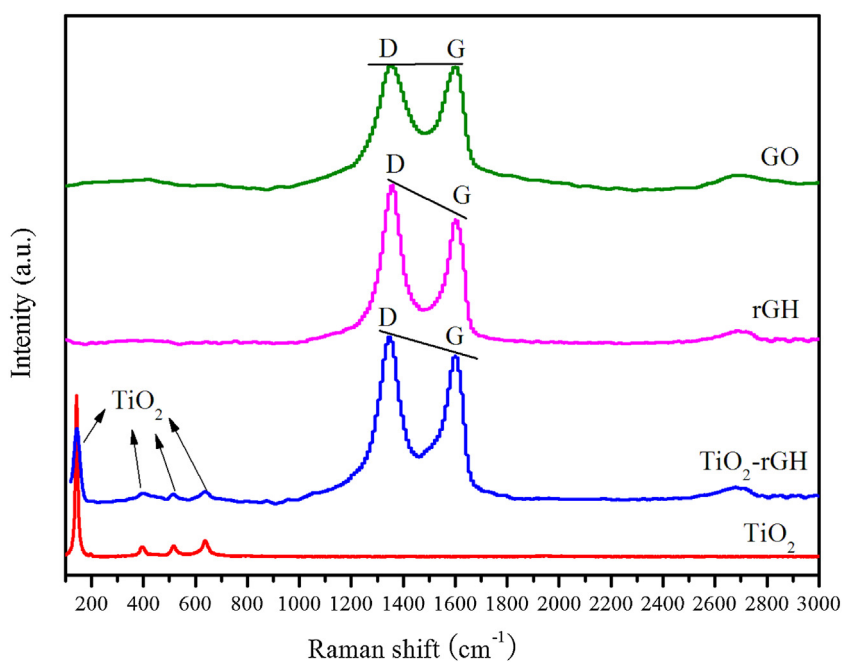


Fig. 2. Raman spectra of GO, rGH, TiO₂, and TiO₂-rGH.

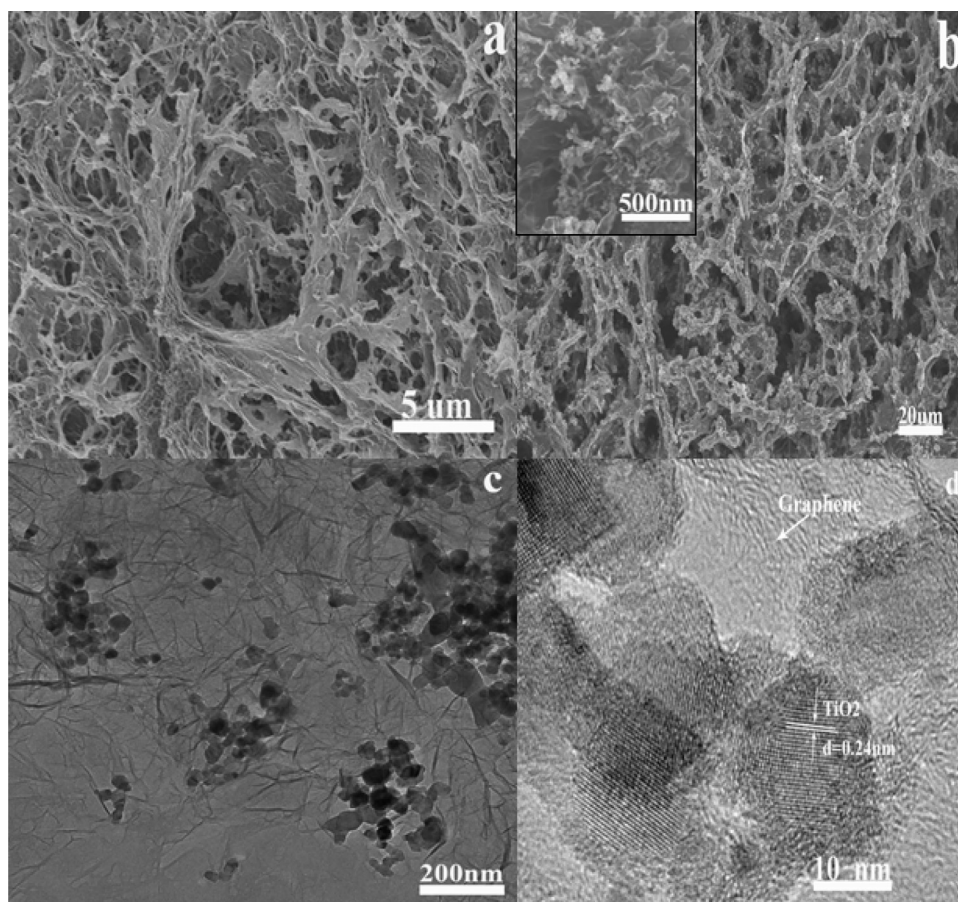


Fig. 3. SEM and TEM studies of rGH and TiO₂-rGH. (a) SEM image of rGH. (b) SEM image of TiO₂-rGH. (c) Low magnification TEM image of TiO₂-rGH. (d) High magnification TEM image of TiO₂-rGH.

in a fixed bed reactor as shown in Fig. 9. The fixed bed reactor for continuous flow reaction is a polyfluorotetraethylene groove (40 mm × 20 mm × 2 mm), equipped an inlet & outlet in the two sides with membranes, and a quartz glass was fixed above the groove. 250 mg of TiO₂-rGH was immobilized in the reactor. The flow rate of the Cr(VI) solution was controlled by a peristaltic pump. The mercury lamp was used as the UV light source.

The contact time is the main parameter for modeling of removing Cr(VI) under continuous flow conditions, which determine the investment and operating costs for a defined removal rate and the contaminant concentration level:

$$Thecontacttime = \frac{m_v}{Q_v}$$

where m_v is the amount of TiO₂-graphene hydrogel (mL) and Q_v is the effluent volumetric flow rate (mL/min).

The concentration of total Cr was determined by an inductively coupled plasma (ICP) direct reading spectrometer. The concentration of Cr(VI) was determined by the diphenyl hydrazine method [21], and the concentration of Cr(III) was calculated by subtracting the Cr(VI) concentration from the total Cr concentration.

3. Results and discussion

3.1. The 3D network gel structure of TiO₂-graphene hydrogel

The synthesis of TiO₂-rGH hydrogel was illustrated in Scheme 1. First, the TiO₂ (P25) was mixed with an equal volume of polyethylene glycol (PEG) 200 and the mixture was grinded to allow for fully mixing. The PEG is a good dispersing agent [22], which could make

TiO₂ nano-powders highly dispersed. Then, GO was added into the mixture, followed by ultra-sonication for about 30 min, and sodium ascorbate was added into the mixture. The sodium ascorbate is the reducing agent, which could reduce the GO to rGO [23] and could also be confirmed in FT-IR spectroscopy FigureS1. The resulting mixture was stirred for 30 min and heated at 95 °C for 60 min, and a cross-linking framework structure was occurred through the overlapping and coalescence among the graphene sheets to hydrogels due to the π - π conjugation [24,25] and the regional diminish of the oxygenic functional groups. Obviously, inhibition of the restacking of graphene sheets was achieved by the TiO₂ nano-powders on the surface may cause steric hindrance and reduce the restacking of graphene sheets to build 3D TiO₂-rGH hydrogel.

XRD was used to investigate the structures of GO, rGH, TiO₂, and TiO₂-rGH (Fig. 1). Oxidation treatment of graphite resulted in a 001 diffraction peak at 12.1°, characteristic of the loose-layer structure of GO. The interlayer space was estimated to be 0.76 nm, larger than that of graphite. This increase was caused by the introduction of a large number of oxygen-containing groups into the graphite structure. A weak 002 diffraction peak was observed at 24.5° for rGH, indicating the corresponding interlayer space of about 0.36 nm. Similar results were also reported in XRD studies [26]. TiO₂-rGH exhibited two crystal forms: a dominant anatase phase marked at 25.3°, 37.8°, 48.0°, 53.9°, 62.7°, 68.9°, 70.3°, and 75.0° (JCPDS#21-1272) [27] and a rutile phase marked at 27.2° and 55.1° (JCPDS#21-1276) [28]. No diffraction peaks of rGH were observed in the TiO₂-rGH sample, which might be due to the fact that rGH was dispersed on the surface of the composite material and a thin coating layer was difficult to detect.

Table 1
Physical and chemical parameters of different adsorbent samples.

| Sample | S_{BET} (m^2/g) | Pore volume (cm^3/g) | Average pore diameter (nm) |
|---------------------------|--|--|----------------------------|
| Graphite | 2.75 | 0.001 | 1.02 |
| rGH | 323.9 | 0.082 | 9.26 |
| TiO ₂ | 46.9 | 0.003 | 9.21 |
| 20% TiO ₂ -rGH | 437.6 | 0.074 | 3.92 |
| TiO ₂ /AC | 165.2 | 0.461 | 2.91 |

Fig. 2 shows the Raman spectra of GO, rGH and the TiO₂-rGH composite. All these samples exhibited two strong peaks, denoted as the disorder peak (D, centered at 1350 cm^{-1}) and the graphitic peak (G, at 1580 cm^{-1}). The D peak suggests the disruption of the symmetrical hexagonal graphitic lattice, which is associated with the internal structure. The G peak indicates the in-plane stretching motion of symmetric sp^2 C–C bond [29]. Compared with the $I_{\text{D}}/I_{\text{G}}$ value of GO, the $I_{\text{D}}/I_{\text{G}}$ value of rGH is increased, suggesting that the oxygen-containing groups were reduced [30]. On the Raman spectra of TiO₂-rGH, the peaks around 388 , 495 and 620 cm^{-1} were assigned to anatase TiO₂ [31]. The D and G peaks were still present, indicating that the TiO₂-rGH composite contained both rGH and TiO₂, consistent with the XRD result. The $I_{\text{D}}/I_{\text{G}}$ value of TiO₂-rGH is similar to that of rGH. Notably, the anatase vibration mode usually results in a sharp Raman peak at 143 cm^{-1} , independent of the nanoparticles. This Raman peak of TiO₂ was observed at 143 cm^{-1} , whereas that of TiO₂-rGH was shifted to 140 cm^{-1} , indicating that the interaction of rGH and TiO₂ generated new types of chemical bonds [32]. The surface functional groups of the TiO₂-rGH were also confirmed by FT-IR analysis in Supporting Information, Fig. S1.

The morphologies, crystal phases, and compositions of different samples were determined by SEM and TEM. As shown in Fig. 3a, the 3D structure rGH not only retained the large accessible surface area of graphene but also exhibited highly connected pores with the size of several micrometers. It also can be confirmed the partial overlapping and crosslinks of between rGO in Fig. 3a. The formation of this unique structure might be caused by the intermolecular forces including π - π conjugation and hydrophobicity between the rGO sheets [33]. The SEM image in Fig. 3b clearly shows that TiO₂ nanospheres were uniformly dispersed on the rGO sheets. The TEM image of TiO₂-rGH shows the lamellar structure of rGH with some chiffon-like ripples and wrinkles with TiO₂ nanospheres in the size of 20 nm uniformly dispersed on the rGO sheets (Fig. 3c). As shown in the high-resolution TEM image (Fig. 3d), these TiO₂ nanoparticles were in intimate contact with rGH and the TiO₂ nanoparticles were in a crystalline anatase phase. The lattice fringes of the TiO₂ nanoparticles had an interlayer space of 0.24 nm , in agreement with the spacing of the (004) planes of TiO₂ and consistent with the JCPDS card no. 21-1272 [34].

N₂ sorption isotherms analysis was conducted to determine the porosity of TiO₂-rGH. As shown in Table 1 and Fig. S3, the results showed that the graphene possesses the specific surface area of $437.6\text{ m}^2\text{ g}^{-1}$ in the composite of TiO₂-rGH hydrogel, which is higher than that of pure rGH ($323.9\text{ m}^2\text{ g}^{-1}$). This could be attributed to the TiO₂ nano-spheres on graphene sheets which could act as pillars and effectively separate the graphene sheets from aggregation, thus increasing the specific surface area of graphene in TiO₂-rGH hydrogel. The functionalized porous 3D network structures of TiO₂-rGH with enhanced surface area of graphene and connected porous channel possesses the advantages of separation free, highly capacity adsorption and photocatalytic reduction in removing Cr(VI) from aqueous solutions.

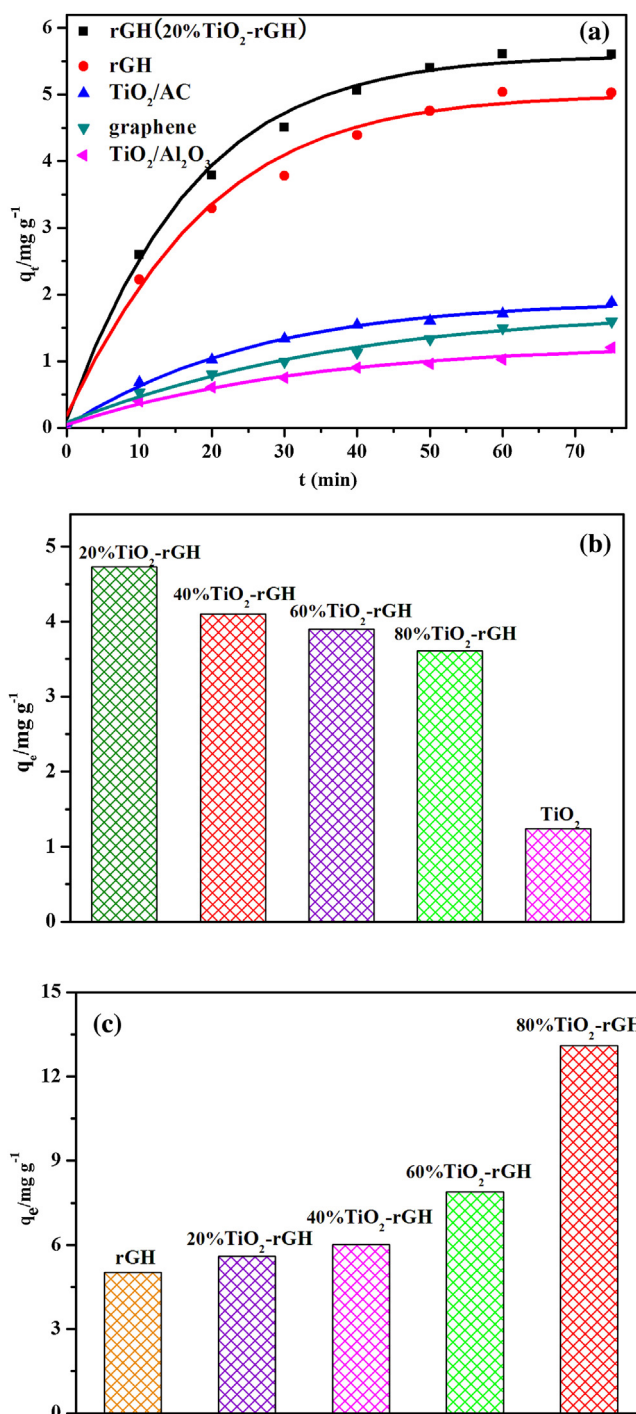


Fig. 4. (a) Cr(VI) adsorption capacity of different composite materials. (b) Cr(VI) adsorption capacity of different TiO₂-rGH hydrogels. (c) Cr(VI) adsorption capacity of Graphene in different TiO₂-rGH hydrogels.

3.2. The adsorption, regeneration ability

The adsorption performance of the 20% TiO₂-rGH, rGH, graphene, TiO₂/AC and TiO₂/Al₂O₃ for Cr(VI) was compared as shown in Fig. 4a. It is evident that the adsorption maxima of 20% TiO₂-rGH and rGH were reached within 60 min. The q_m values of 20% TiO₂-rGH and rGH were 5.60 and 5.03 mg/g , respectively. The adsorption rate of TiO₂/AC and TiO₂/Al₂O₃ was slow compared to those of 20% TiO₂-rGH and rGH. The absorption maxima

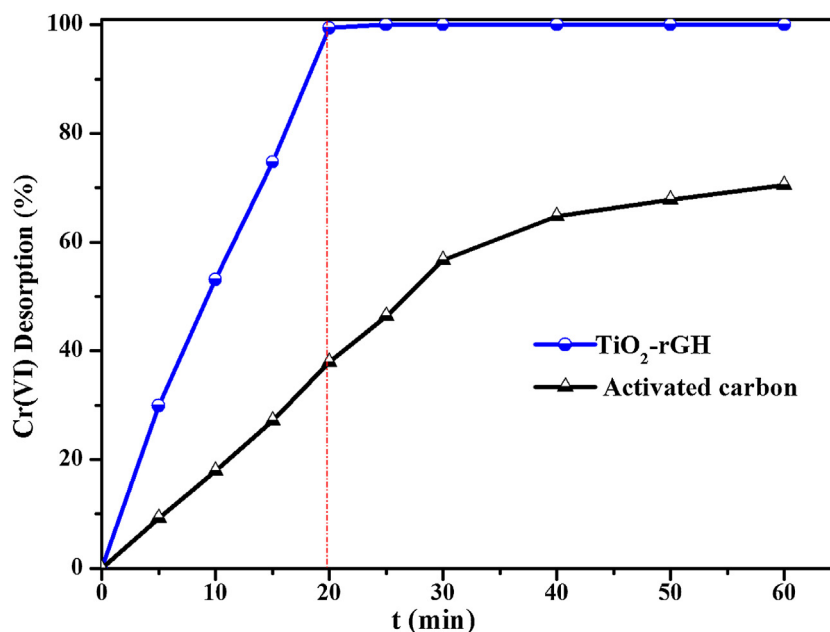


Fig. 5. Comparison of the desorption of TiO₂-rGH and activated carbon.

of TiO₂/AC and TiO₂/Al₂O₃ were reached after 180 min with the q_m values as 1.88 and 1.20 mg/g, respectively, smaller than those of 20% TiO₂-rGH and rGH. Overall, TiO₂-rGH exhibited the best adsorption performance. This result may be attributed to the fact that the enhanced surface area of graphene in the 3D structure of TiO₂-rGH hydrogel (Table 1). Compared with conventional adsorbent materials, the TiO₂-rGH composite hydrogel material possesses a unique three-dimensional network structure with the highly adsorption capacity.

The Cr(VI) adsorption capacity of different TiO₂-rGH samples was investigated and the result is shown in Fig. 4b. The q_m values of the samples containing 20%, 40%, 60%, 80%, and 100% TiO₂ were 4.73, 4.10, 3.90, 3.61, 1.24 mg/g, respectively. Thus, the content of TiO₂ had a great influence on the adsorption capacity of the hydrogel composites. A similar set of samples with varying amounts of rGH was also studied (Fig. 4c). The q_m values of the samples containing 20%, 40%, 60%, and 80% TiO₂ were determined as 5.60, 6.01, 7.89, and 13.09 mg/g, higher than that of rGH (5.03 mg/g). In TiO₂-rGH, the TiO₂ nanoparticles effectively prevented the aggregation of the GO sheets, which influenced the growth of the 3D TiO₂-rGH structure [35], and thus improved the surface area of rGO. Another key factor in generating the adsorption capacity of TiO₂-rGH is the graphene π - π interactions, which reduced the competitive adsorption of water [36].

Conventional adsorbent materials, such as activated carbon (AC), mainly rely on the adsorption active sites and interlayer adsorption sites within the pores, which limits the adsorption rate and renewable ability. The desorption activities of TiO₂-rGH and activated carbon were performed by nitric acid elution, which are shown in Fig. 5. In the case of TiO₂-rGH, all of Cr(VI) was eluted after ca. 20 min, whereas only 70.5% Cr(VI) was eluted over activated carbon after 60 min, evidently revealing that the TiO₂-rGH hydrogel structure has a rapid adsorption and desorption ability and the separation free character, which is a key point for the recycling and regeneration of adsorption materials. The non-porous surface adsorption and π - π interaction adsorption of graphene and the 3D network hydrogel structure are considered for the main reasons of enhanced adsorption and desorption in removing of Cr(VI).

3.3. The synergy of adsorption and photocatalysis in a static system

The photocatalytic activity of each adsorbent material was investigated by evaluating the reduction rate of Cr(VI) under UV light. Fig. 6a shows the photocatalytic activity of TiO₂, TiO₂-rGH, rGH, TiO₂/AC, TiO₂/Al₂O₃ and a blank test. During the dark period, TiO₂, rGH, TiO₂-rGH, TiO₂/AC and TiO₂/Al₂O₃ removed Cr(VI) from the solution via adsorption. The adsorption equilibrium was reached between 60 and 90 min for these materials. The adsorption percentage at 90 min was 12%, 47%, 50%, 18% and 13.5%, respectively. Upon UV irradiation, TiO₂, TiO₂-rGH, TiO₂/AC and TiO₂/Al₂O₃ catalyzed the reduction of Cr(VI) to Cr(III), causing a decrease in the concentration of Cr(VI). After 90 min, the removal Cr(VI) percentage of TiO₂, TiO₂/AC, and TiO₂/Al₂O₃ was 73.6%, 84.8% and 80.0%, respectively, lower than that of TiO₂-rGH. In contrast, rGH was incapable of photocatalysis. In the TiO₂-rGH sample, all of Cr(VI) were removed after 60 min UV irradiation and exhibited a synergy of adsorption and photocatalysis. Conventional adsorbent materials, such as activated carbon composite, mainly rely on the adsorption active sites and interlayer adsorption sites within the pores, limiting the adsorption rate and renewable ability. In contrast, the TiO₂-rGH composite hydrogel material possesses a unique three-dimensional network structure and non-porous surface adsorption with the highly adsorption capacity.

The influence of different composite materials (i.e., TiO₂-rGH, TiO₂/AC, and TiO₂/Al₂O₃) on the adsorption-photocatalysis synergistic effect was investigated (Fig. 6b). Under UV irradiation, TiO₂-rGH removed 100% Cr(VI) from the water solution within 30 min. Other samples reached equilibrium on or before 70 min, later than TiO₂-rGH. At 70 min, the removal percentage of TiO₂, rGH, TiO₂/AC, and TiO₂/Al₂O₃ was 73.6%, 49.0%, 84.8% and 80.0%, respectively, lower than that of TiO₂-rGH. Therefore, TiO₂-rGH displayed better performance in removing Cr(VI) than other composite materials, such as TiO₂/AC and TiO₂/Al₂O₃.

Fig. 7a shows the performance of different TiO₂-rGH samples in removing Cr(VI) from the water solution. It seemed that a higher content of TiO₂ could cause a decrease in the adsorption capacity and an increase in the photocatalytic rate. Nonetheless,

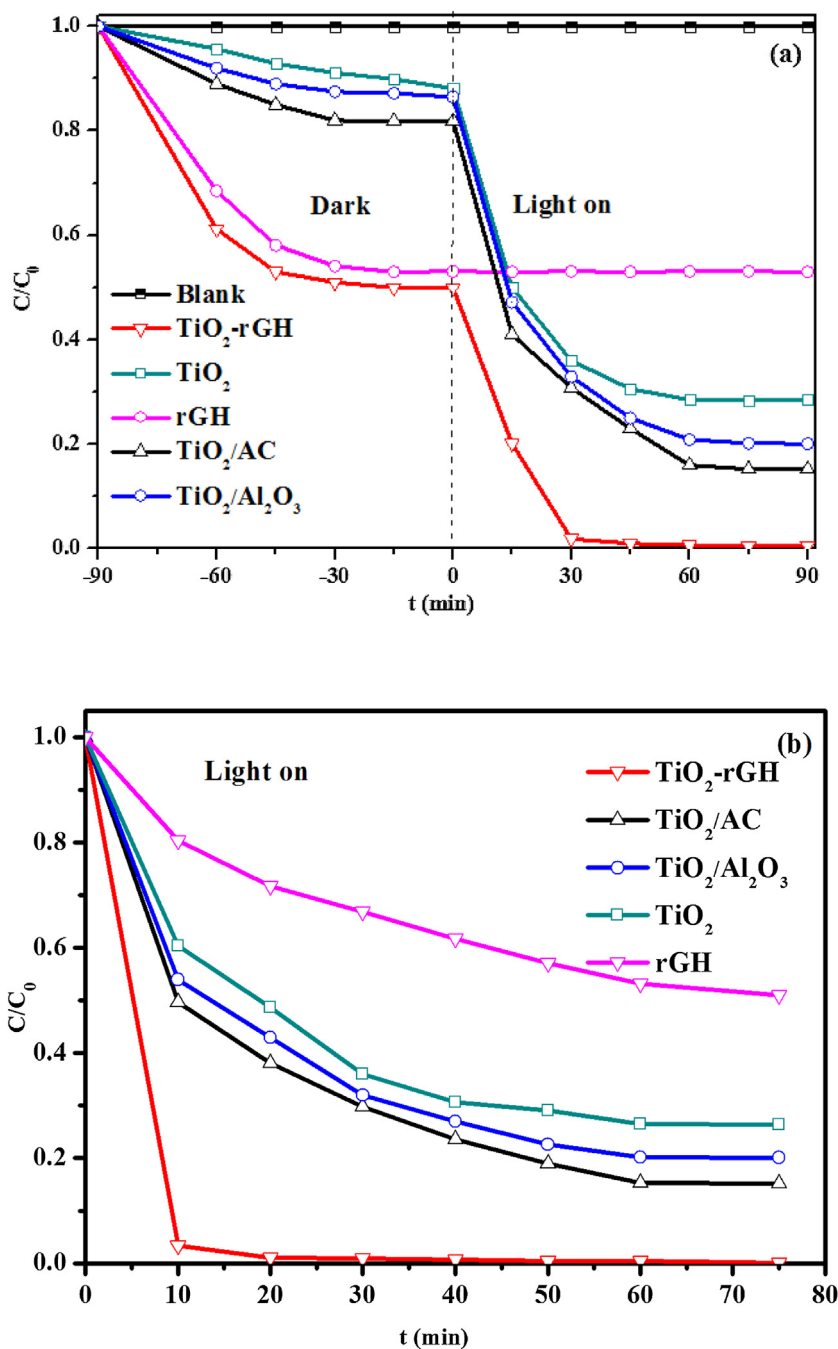


Fig. 6. (a) Comparison of photocatalytic activity of TiO_2 , $\text{TiO}_2\text{-rGH}$, and rGH in reducing Cr(VI). (b) Influence of different composite materials on the adsorption-photocatalysis synergistic effect.

all these $\text{TiO}_2\text{-rGH}$ samples presented a very good adsorption-photocatalysis performance in removing Cr(VI), and nearly 100% Cr(VI) was removed at 60 min. At different Cr(VI) concentrations (i.e., 10, 30, 50, 100, 200 ppm) in Fig. 7(b), the synergy of adsorption and photocatalysis allowed $\text{TiO}_2\text{-rGH}$ to remove Cr(VI) rapidly and efficiently. At 20 min, the removal percentage was in the range of 85–100%. In contrast, the removal percentage of adsorption alone was in the range of 15–47% when the adsorption equilibrium was reached in the dark within 60 min. Although photocatalysis was effective in reducing Cr(VI), it was slower than the synergy of adsorption and photocatalysis in removing Cr(VI). It took 150 min to reach a similar level of the removal percentage (70–100%) com-

pared to the combination of adsorption and photocatalysis (see Fig. S6).

The reuse ability is essential for the practical application of photocatalysis. The recycling runs of the $\text{TiO}_2\text{-rGH}$ composite material in removing Cr(VI) was evaluated, as shown in Fig. 8. Each cycle run is followed by another cycle run without any elution or desorption. Both the adsorption process and the adsorption-photocatalysis process were performed. As for adsorption process, only ca. 10% of Cr(VI) removing ability was remain after 5 cycle run in the adsorption performance, indicating that the adsorption sites were occupied by Cr(VI) which could not be further moved. In the adsorption-photocatalysis process, although the removing ability of Cr(VI) was slightly decreased after each cycle run, more than

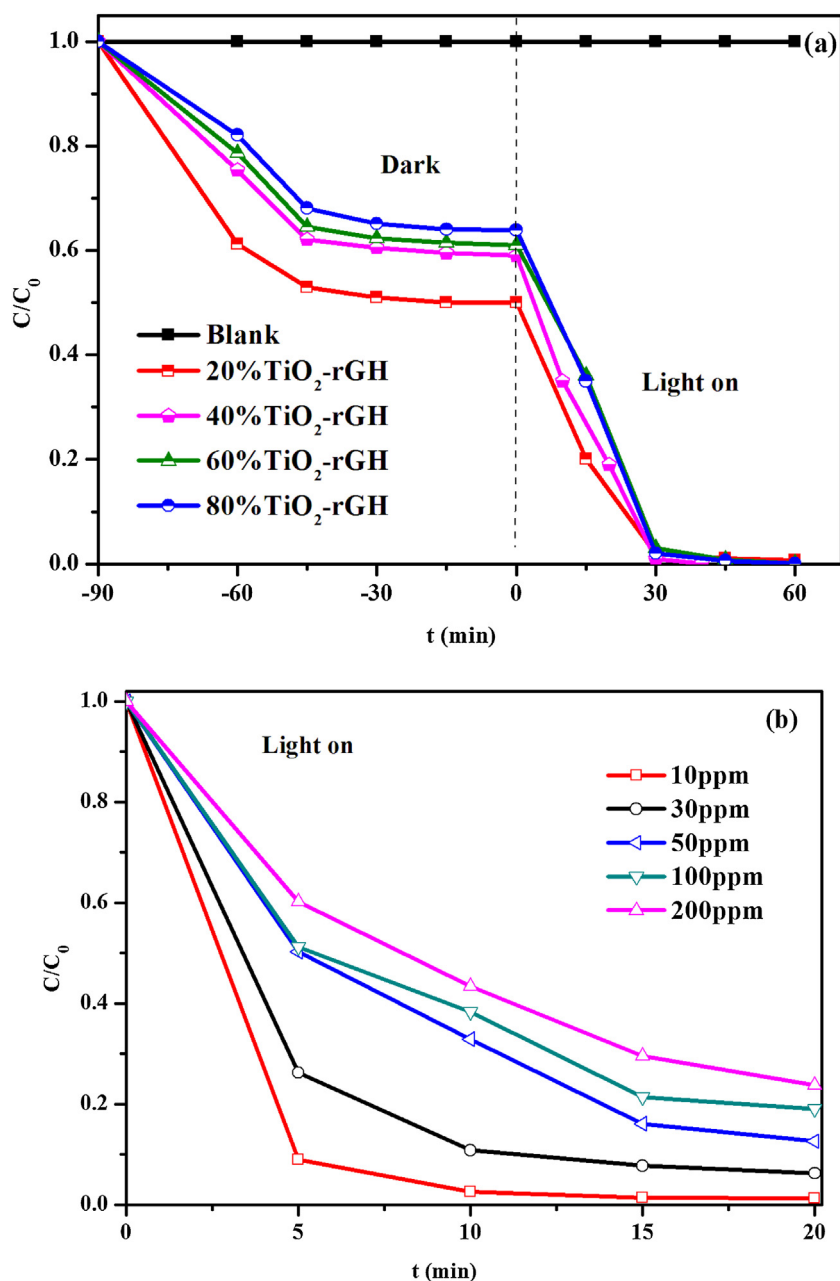


Fig. 7. (a) Adsorption-photocatalytic performance of different TiO₂-rGH samples. (b) Adsorption-photocatalysis performance of TiO₂-rGH at different Cr(VI) concentrations.

90% Cr(VI) removing ability was still remained after five cycle runs, indicating that the adsorbed Cr(VI) by graphene could be further reduced through photocatalysis process by TiO₂, showing a high recycle, renewable and separation free ability. Thus, the synergy of adsorption and photocatalysis significantly improved the reusability and maintained the performance of TiO₂-rGH under continuous working conditions.

3.4. The synergy of adsorption and photocatalysis in a continuous flow system

The performance of the TiO₂-rGH composite material in removing Cr(VI) under continuous flow conditions was further performed in a fixed bed reactor as shown in Fig. 9. The results are shown in Fig. 10, the adsorption percentage of Cr(VI) started to drop at 3 h when the adsorption sites of TiO₂-rGH gradually became saturated. After 18 h, the TiO₂-rGH composite material was completely satu-

rated and no adsorption of Cr(VI) was observed. In contrast, the adsorption-photocatalysis performance remained constant within 15 h under the same experimental conditions. After 15 h, the Cr(VI)-removing efficiency started to decrease until a new equilibrium state was reached (Cr(VI)-removing efficiency: 86%).

The adsorption-photocatalysis performance of TiO₂-rGH at different Cr(VI) concentrations under continuous flow conditions was investigated. As shown in Fig. 11, an increase in the Cr(VI) concentration made the system reach the breakthrough point ahead of time. In the presence of 2, 5, and 10 mg/L Cr(VI), the breakthrough point was 15, 10, and 3 h, respectively. Thus, the concentration of Cr(VI) had a great influence on the adsorption-photocatalysis performance of TiO₂-rGH. A higher concentration of Cr(VI) possesses higher diffusion coefficient, resulting in a faster transport of Cr(VI) from solution onto TiO₂-rGH, so that an earlier breakthrough point was occurred in the high concentration of Cr(VI). After the breakthrough point, the Cr(VI)-removing efficiency started to decrease

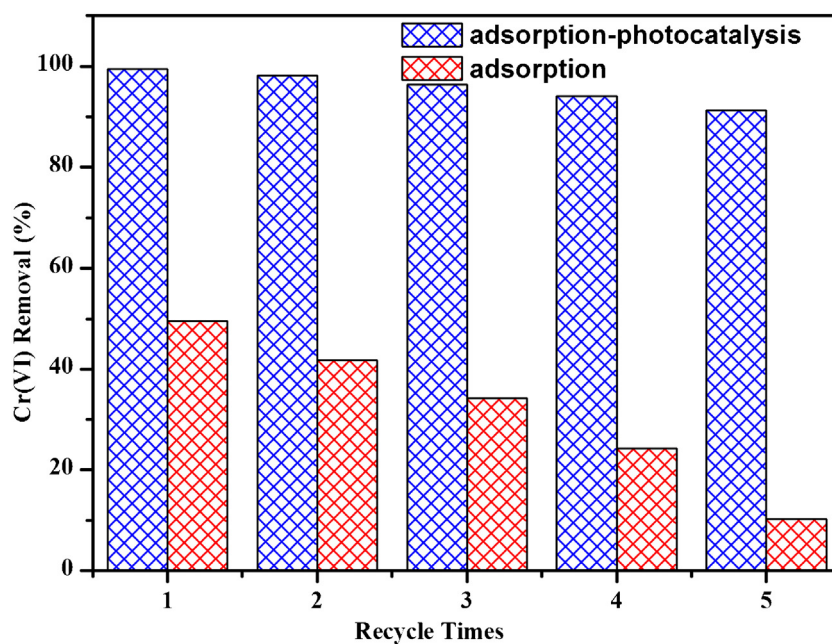


Fig. 8. Recycling runs of TiO_2 -rGH in removing Cr(VI) without desorption.

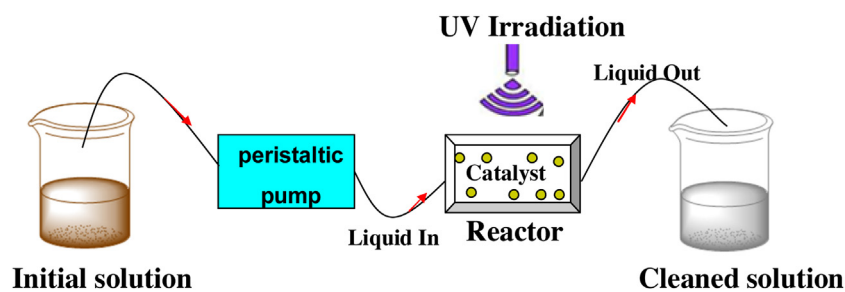


Fig. 9. Schematic diagram of the continuous flow setup.

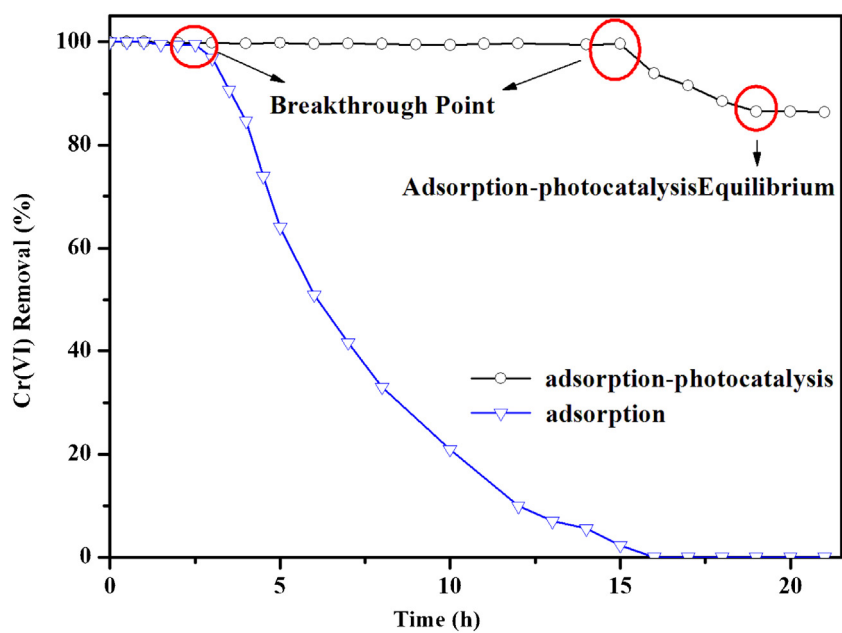


Fig. 10. Performance of TiO_2 -rGH under continuous flow conditions.

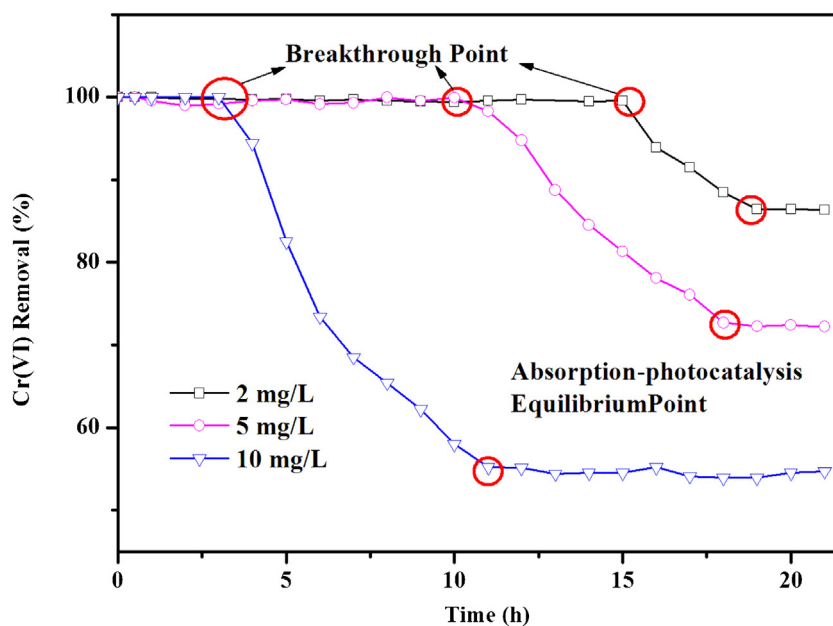


Fig. 11. Adsorption-photocatalysis performance of TiO_2 -rGH at different Cr(VI) concentrations under continuous flow conditions.

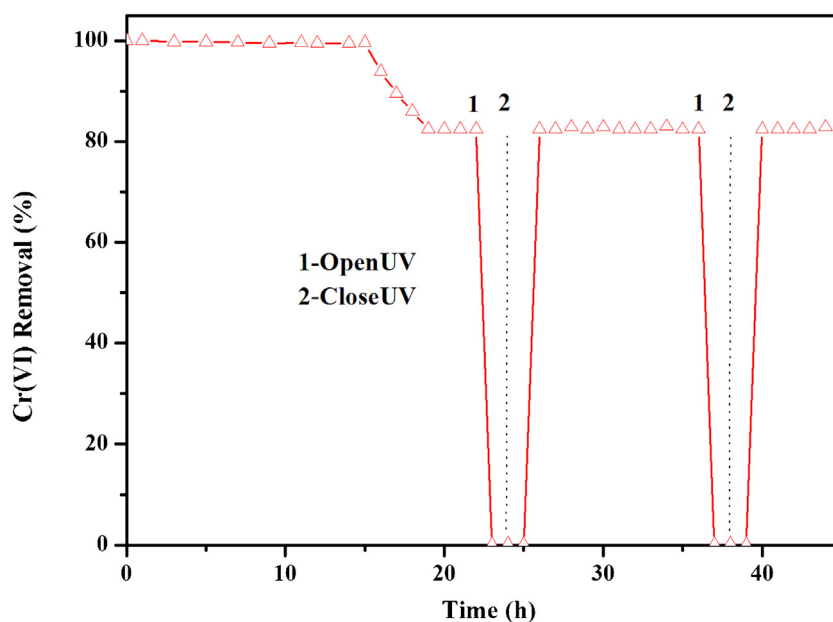


Fig. 12. Performance of TiO_2 -rGH at alternating dark-light cycles under continuous flow conditions.

until the equilibrium point was reached. The Cr(VI) -removing efficiency at the equilibrium point was 83%, 72%, and 54%, respectively. Similar results were observed when the flow rate was gradually increased (see Fig. S7).

Fig. 12 shows the performance of TiO_2 -rGH at alternating dark-light cycles under continuous flow conditions. It is evident that the Cr(VI) removing was completely stopped upon removing the UV irradiation, indicating that the adsorption sites of TiO_2 -rGH were saturated after the equilibrium point. Re-introducing the UV irradiation brought the Cr(VI) -removing efficiency to the original level at the equilibrium point, demonstrating a stable photocatalysis reaction of Cr(VI) on the TiO_2 -rGH surface. The TiO_2 -graphene hydrogel with 3D network structure has the advantage of good adsorption performance and catalyzed the reduction of Cr(VI) to Cr(III) in situ, thereby reducing the toxicity of heavy metal ions in water, and

separation-free characters, indicating that this composite hydrogel can continuously purify for waste water and does not need to separate and regenerate.

3.5. Mechanism

The mechanism of TiO_2 -rGH-mediated removal of Cr(VI) from the water solution are described as shown in Fig. 13. SEM and TEM studies showed that the TiO_2 nanospheres were uniformly dispersed on the 3D GO sheets. These nanospheres acted as pillars and effectively separated the GO sheets from each other. As a result, the specific surface area of rGH was increased, generating more adsorption sites. In addition, the oxygen-containing functional groups in GO provided a lot of chemical adsorption sites. In aqueous environments (the pH of the Cr(VI) solution is about 5.5), Cr(VI) is usually

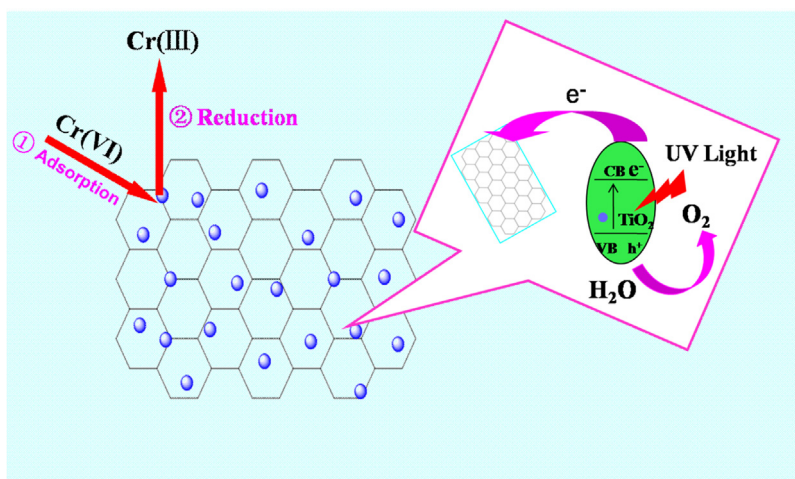
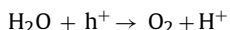
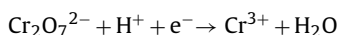
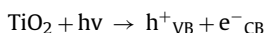


Fig. 13. Schematic diagram of TiO₂-rGH-mediated removal of Cr(VI).

present in the forms of HCrO_4^- and CrO_4^{2-} [37,38]. The surface of TiO₂-rGH was positively charged and confirmed in Fig. S4 (Zeta potential analysis of TiO₂-rGH), which favored the uptake of Cr(VI) anions through electrostatic attraction. The combination of rGH and TiO₂ nanospheres promoted photo-induced charge transport and separation, facilitating photocatalytic reduction of Cr(VI). A mechanism for the synergy of adsorption- photocatalysis was proposed. First, Cr(VI) contaminant was adsorbed by graphene hydrogel through the 3D network structure of TiO₂-graphene hydrogel. Then the Cr(VI) contaminant was further photocatalytic reduced to form Cr(III) [39,40] by photo-induced electrons under UV light irradiation. Meanwhile, the remaining holes would oxidize the water to produce oxygen and hydrogen ions, which could continue to participate in the reduction reaction of Cr(VI) [41]. It can be considered that the photo-induced electrons and holes have good coordination to promote the reduction of Cr(VI) to Cr(III). The possible mechanism of the photocatalytic reduction of hexavalent chromium is as follows:



The synergy of adsorption and photocatalysis for TiO₂-graphene hydrogel achieved the aim of removing of Cr(VI) and in situ regeneration of materials, so that ensure the continuous removing of heavy metal ions from aqueous solutions.

4. Conclusion

In summary, a novel TiO₂-graphene hydrogel with three-dimensional (3D) network structure has been fabricated. This 3D hydrogel structure exhibited superb adsorption-photocatalysis performance for removing Cr(VI) from aqueous solutions. 100% Cr(VI) from a solution containing (5 mg/L) could be removed within 30 min by the synergy performance of adsorption and photocatalysis. Under continuous flow conditions, the Cr(VI)-removing percentage was kept at 100% for a prolonged period until the breakthrough point was reached. The strengthened performance can be attributed to the non-porous surface adsorption and π - π interaction adsorption for graphene, and the combination between graphene and TiO₂ nanospheres promoted photo-induced charge transport and separation, thereby facilitating photocatalytic reduction of Cr(VI). A mechanism for the synergy of

adsorption- photocatalysis was proposed. First, Cr(VI) contaminant was adsorbed by graphene hydrogel through the 3D network structure of TiO₂-graphene hydrogel. Then the Cr(VI) contaminant was photocatalytic reduced by TiO₂ under UV light irradiation, so that realized the rapid in situ regeneration. The TiO₂-graphene hydrogel with 3D network structure has the advantage of high Cr(VI) removing ability and separation-free, which could continuously purify the waste water. Overall, our work provides new insights into the fabrication of hydrogel-based nanocomposites and facilitates their potential application for the synergistic removal of various aquatic pollutants in the field of water purification.

Acknowledgements

This work was partly supported by National Basic Research Program of China (973 Program) (2013CB632403) and the National Natural Science Foundation of China (21437003, 51372068), Hebei Natural Science Funds for Distinguished Young Scholar (grant No. B2014209304).

Appendix A. Supplementary data

Supplementary data associated with this article can be found, in the online version, at <http://dx.doi.org/10.1016/j.apcatb.2016.06.053>.

References

- [1] B. Jiang, Y.K. Liu, J.T. Zheng, M.G. Tan, Z.H. Wang, M.B. Wu, *Environ. Sci. Technol.* 49 (2015) 12363–12371.
- [2] Y. Huang, C.R. Li, Z. Lin, *Appl. Mater. Interfaces* 6 (2014) 19766–19773.
- [3] Y.X. Yu, *Appl. Mater. Interfaces* 6 (2014) 16267–16275.
- [4] M.A. Worsley, T.T. Pham, A.M. Yan, S.J. Shin, J.R.I. Lee, M. Bagge-Hansen, W. Mickelson, A. Zettl, *Nano* 8 (2014) 11013–11022.
- [5] Z.Y. Sui, Y. Cui, J.H. Zhu, B.H. Han, *Appl. Mater. Interfaces* 5 (2013) 9172–9179.
- [6] D. Zhang, B. Pan, H. Zhang, *Environ. Sci. Technol.* 44 (2010) 3806–3811.
- [7] F.K. Meng, S.K. Cushing, J.T. Li, S.M. Hao, N.Q. Wu, *ACS Catal.* 5 (2015) 1949–1955.
- [8] E. Antolini, *Appl. Catal. B* 88 (2009) 1–24.
- [9] Y.Y. Li, Y. Ding, *Phys. Chem. C* 114 (2010) 3175–3179.
- [10] K.S. Novoselov, A.K.S.V. Geim, Morozov, *Sci.* 306 (2004) 666–669.
- [11] X.H. Jiang, W.X. Yu, D.W. Cao, G.W. Zhou, *Environ. Sci. Technol.* 3 (2007) 20–28.
- [12] S.D. Zhuang, X.Y. Xu, B. Feng, J.G. Hu, Y.R. Pang, G. Zhou, L. Tong, Y.X. Zhou, *Appl. Mater. Interfaces* 6 (2014) 613–621.
- [13] K. Jeonhwan, P. Hongsik, B.H. James, W.B. Stephen, F.D.K.S. Keith, *Science* 342 (2013) 833–836.
- [14] D. Diptiman, G. Abhisek, K.S. Shyamal, *Mater. Chem. A* 1 (2013) 11221–11228.
- [15] M. Motoi, M. Tomohide, T. Hideki, *Carbon* 44 (2006) 2681–2688.
- [16] L. Petr, K. František, J. Petr, K. Mikuláš, O. Eva, S. Klára, O. Michal, *Am. Chem. Soc.* 135 (2013) 6372–6377.

- [17] Y.X. Xu, K.X. Sheng, C. Li, G.Q. Shi, *Nano* 4 (2010) 4324–4330.
- [18] J.N. Tiwari, K. Mahesh, N.H. Le, *Carbon* 56 (2013) 173–182.
- [19] J. Xu, L. Wang, Y.F. Zhu, *Langmuir* 28 (2012) 8418–8425.
- [20] S. Humaira, S. Muhammad, H.L. Nhien, *Nanoscale* 5 (2013) 3149–3171.
- [21] B. Jiang, Y.K. Liu, J.T. Zheng, M.H. Tan, Z.H. Wang, M.B. Wu, *Environ. Sci. Technol.* 49 (2015) 12363–12371.
- [22] M. Gaberell, Y.P. Chin, S.J. Hug, B. Sulzberger, *Ultrason. Sonochem.* 18 (2011) 1197–1204.
- [23] S. Mao, G.H. Lu, J.H. Chen, *Nanoscale* 7 (2015) 6924–6943.
- [24] H. Hu, Z.B. Zhao, W.B. Wan, Y. Gogotsi, J.S. Qiu, *Adv. Mater.* 25 (2013) 2219–2223.
- [25] F. Liu, S.Y. Song, D.F. Xue, H.J. Zhang, *Adv. Mater.* 24 (2012) 1089–21094.
- [26] W.J. Han, L. Ren, L.J. Gong, X. Qi, Y.D. Liu, L.W. Yang, X.L. Wei, J.X. Zhong, *Sustainable Chem. Eng.* 5 (1996) 741–748.
- [27] N. Takeda, T. Torimoto, S. Sampath, *J. Phys. Chem.* 24 (1995) 9986–9991.
- [28] J. Du, X.Y. Lai, N.L. Yang, *ACS Nano* 5 (2011) 590–596.
- [29] I.V. Lightcap, T.H. Kosel, P.V. Kamat, *Nano Lett.* 10 (2010) 577–583.
- [30] H.P. Cong, X.C. Ren, P. Wang, *ACS Nano* 6 (2012) 2693–2703.
- [31] W.F. Zhang, Y.L. He, M.S. Zhang, *J. Phys. D Appl. Phys.* 33 (2000) 912–916.
- [32] X. Pan, Y. Zhao, S. Liu, *ACS Appl Mater Inter.* 4 (2012) 3944–3950.
- [33] X. Cai, S.Z. Tan, M.S. Lin, A.G. Xie, W.J. Mai, X.J. Zhang, *Langmuir* 27 (2011) 7828–7835.
- [34] A. Srinivasan, N.R. Tata, S. Marappan, R. Dinesh, H. Itaru, M. Masahiro, *Appl. Mater. Interfaces* 5 (2013) 207–212.
- [35] Z.Y. Zhang, F. Xiao, Y.L. Guo, S. Wang, Y.Q. Liu, *Appl. Mater. Interfaces* 5 (2013) 2227–2233.
- [36] K.S.W. Sing, D.H. Everett, R.A.W. Haul, *Pure Appl. Chem.* 57 (1985) 603–619.
- [37] M. Gaberell, Y.P. Chin, S.J. Hug, B. Sulzberger, *Environ. Sci. Technol.* 37 (2003) 4403–4409.
- [38] Y. Hiroshi, Y. Yukiyasu, T. Hideo, *Nature* 282 (1979) 817–818.
- [39] H.Y. Li, T.S. Wu, B. Cai, W.G. Ma, Y.J. Sun, S.Y. Gan, D.X. Han, L. Niu, *Appl. Catal. B* 164 (2015) 344–351.
- [40] Y.Y. Fan, W.G. Ma, D.X. Han, S.Y. Gan, X.D. Dong, L. Niu, *Adv. Mater.* 27 (2015) 3767–3773.
- [41] P. Mohapatra, S.K. Samantaray, K. Parida, J. Photochem. Photobiol. A 170 (2005) 189–194.